Crystal structure, optical properties and thermal properties of $M_2[W_2O_3(SO_4)_6]$ (M = Y, Eu, Tb, Lu, Bi)†

Vivien Wessels, Sofia Kügle and Henning A. Höppe *

Sulfatotungstates constitute a rather new host structure materials that may exhibit interesting optical properties. The compounds $M_2[W_2O_3(SO_4)_6]$, with M = Y, Eu, Tb, Lu, and Bi, were synthesised as phase pure materials under solvothermal conditions in oleum. They crystallise isotypic to each other in the monoclinic space group *C*2/*c* (no. 15) with *Z* = 4, determined by single-crystal X-ray diffraction. Their structures feature corner-connected sulfate and tungstate units, the latter showing a disorder of the tungstate cations with a thread-like arrangement along the *b*-axis. The metal cations M are eight-fold-coordinated and show typical red (M = Eu) or green (M = Tb) luminescence in fluorescence spectra due to their f–f transitions. The f–d transition of Tb^{3+} reveals rather weak coordination behaviour of the host structure. Thermal analysis showed relatively high temperature stabilities of the compounds, increasing as the ionic radii of the metal cations decrease. Additionally, the compounds were characterised by FT-IR and UV-vis measurements while using Tauc plots to determine their band gaps. The lone-pair activity of the bismuth compound was elucidated by geometrical calculations based on the structural data.

Introduction

Our research focuses on the investigation of new silicate-analogue materials with interesting optical properties as promising phosphor materials. Such materials contain tetrahedral building units as a structural motif that lack inversion symmetry. Thus, non-centrosymmetric crystal structures are often formed yielding high luminescence probabilities. They are enhanced by the absence of local inversion centres in host structures due to the parity selection rule; thus, partial mixing of orbitals becomes possible. Tungstates can be classified as silicateanalogues due to their ability to form $[WO_4]^{2-}$ tetrahedral building units in addition to $[WO_7]^{8-}$, $[WO_6]^{6-}$ and $[WO_5]^{4-}$ moieties.[1–5] Their potential as phosphors is particularly intriguing due to the possibility of their acting as an antenna and facilitating energy transfer towards rare-earth elements R, thereby enhancing their f–f-transitions. This effect is particularly observed in tungstates, such as $AR(WO_4)_2$ and $Na_5R(WO_4)_4$ with A = Li, Na, and K and in $Na_2R(PO_4)(WO_4)$, while $[WO_4]^{2-}$ tetrahedral units serve as the antenna.[2,6] Besides, $[WO_6]^{6-}$ octahedral units are also capable of transferring energy towards rare-earth ion activators as observed in compounds such as R_2WO_6.[7]

Rare-earth ions typically exhibit weak ligand-field effects. Silicate-analogue materials, such as sulfates, borophosphates, or borosulfates, feature weak coordination behaviour and are therefore suitable candidates as host structures for rare-earth ions.[8,9] Combining the antenna effect of tungstates with the weak coordination behaviour of sulfates leads to a new capable material class named sulfatotungstates, which presumably possess promising optical properties. Currently, only a limited number of compounds featuring condensed sulfate and tungstate moieties are known, excluding polyoxometalates.[10] In the past decade, the potassium sulfatotungstate $K_8[W_2O_4(SO_4)_6]$ was synthesised in molten mixtures; it constituted the first of its kind, followed by $Rb_8[W_2O_4(SO_4)_6]$.[11–13] More recently, $WO(SO_4)_2$ and $R_2[W_2O_3(SO_4)_6]$ (R = Sm, Eu, Gd, Ho) were synthesised under solvothermal conditions in oleum.[14,15] Neither absorption spectra nor luminescence spectra have been obtained so far for any sulfatotungstates, with only some crystal structures being determined.

This contribution not only introduces new metal cations into the compounds $M_2[W_2O_3(SO_4)_6]$ with M = Y, Eu, Tb, Lu, and Bi. Moreover, a detailed crystal structure determination alongside the optical and thermal properties are elucidated.

Results and discussion

Crystal structure

The compounds $M_2[W_2O_3(SO_4)_6]$ (M = Lu, Y, Tb, Eu, Bi) crystallise isotypic to each other in the monoclinic space group *C*2/*c*

Lehrstuhl für Festkörperchemie, Universität Augsburg, Universitätsstraße 1, 86159 Augsburg, Germany. E-mail: henning.hoeppe@physik.uni-augsburg.de

†Electronic supplementary information (ESI) available. CCDC 2376268–2376272. For ESI and crystallographic data in CIF or other electronic format see DOI: https://doi.org/10.1039/d4dt02259a

(no. 15) with four formula units per unit cell. The respective cell parameters are listed in Table 1. These results were confirmed by X-ray powder diffractometry (see below and in Fig. 3) and Rietveld refinement on the europium compound (Fig. S2, S12 and Table S3 in the ESI†). All atoms, except for the disordered atoms O1A and O1B, are assigned to the general Wyckoff position 8*f*, with the disordered atoms being assigned to the special position 4*e*. The fundamental building unit $[W_2O_3(SO_4)_6]^{6-}$ contains groups of sulfate tetrahedra and tungstate octahedra connected by common edges (Fig. 1a and b), while two tungstate octahedra are connected by a common edge and two bridging sulfate tetrahedra. The remaining four sulfate tetrahedra act as monodentate ligands, while each tungstate octahedron also features a terminal oxygen ion. The charge-balancing metal cation is coordinated by eight oxygen atoms, which form a distorted square antiprism (Fig. 1c). All the coordinating oxygen atoms belong to sulfate tetrahedra of neighbouring $[W_2O_3(SO_4)_6]^{6-}$ units.

While within the *a*-*c*-plane everything looks nicely ordered (Fig. 1a), the tungsten atoms reveal a thread-like arrangement of two almost equivalent sites along the *b*-axis, *i.e.* W1A and W1B (Fig. 2). Both provide octahedral voids yielding essentially the same $[W_2O_3(SO_4)_6]^{6-}$ units. Considering the site occupancy factors in Table 1, the A scenario exhibits a considerably higher occupation probability than the B scenario. The sites

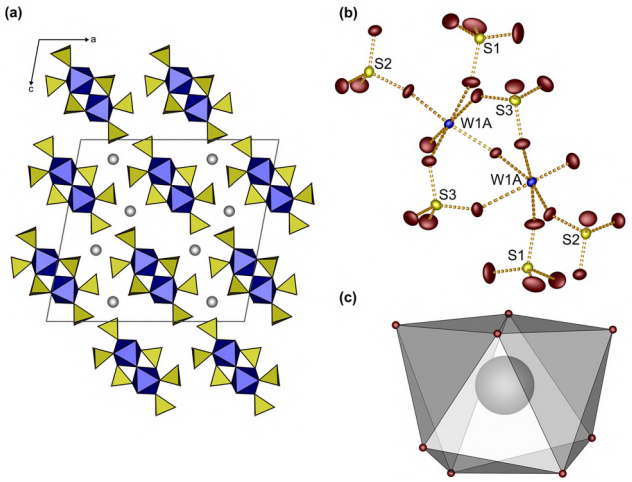

Fig. 1 Unit cell of $Eu_2[W_2O_3(SO_4)_6]$ depicted along the *b*-axis only with W1A disorder (a). Fundamental building unit of the anionic host structure (b). Coordination environment of Eu^{3+} (c). Sulfate tetrahedra, yellow; tungstate octahedra, blue; oxygen ions, red; europium cations, grey; ellipsoids are set to a probability of 80%.

W1A and W1B are not chemically equivalent since the bond lengths and angles towards the oxygen ligands are different; this is also reflected in their respective polyhedron deviations

Table 1 Crystal data and details of the structural refinements determined using single-crystal diffraction. Standard deviations are given in parentheses

	$Y_2[W_2O_3(SO_4)_6]$	$Eu_2[W_2O_3(SO_4)_6]$	$Tb_2[W_2O_3(SO_4)_6]$	$Lu_2[W_2O_3(SO_4)_6]$	$Bi_2[W_2O_3(SO_4)_6]$
Temperature/K	200(2)	300(2)	300(2)	300(2)	200(2)
Molar weight/g mol^{-1}	1169.88	1295.98	1309.90	1342.00	1410.02
Crystal system	Monoclinic	Monoclinic	Monoclinic	Monoclinic	Monoclinic
Space group	*C*2/*c* (no. 15)	*C*2/*c* (no. 15)	*C*2/*c* (no. 15)	*C*2/*c* (no. 15)	*C*2/*c* (no. 15)
a/Å	19.9837(4)	19.981(4)	19.9980(6)	19.930(2)	19.8501(6)
b/Å	5.42800(10)	5.5145(10)	5.4727(2)	5.3595(7)	5.5513(2)
c/Å	18.5278(4)	18.672(3)	18.5827(6)	18.403(2)	18.7720(6)
β/°	100.7050(10)	100.750(7)	100.8300(10)	100.675(5)	100.1480
V/Å^3	1974(76)	2021.2(7)	1997.52(11)	1931.7(4)	2036.20(12)
Z	4	4	4	4	4
ρ/g mol^{-1}	3.935	4.259	4.356	4.614	4.600
Absorption coefficient *μ*/mm^{-1}	18.204	18.221	19.238	22.792	29.245
F(000)	2152	2344	2360	2408	2504
Radiation; wavelength *λ*/Å			Mo-K$_\alpha$; 0.71073		
Diffractometer			Bruker D8 Venture		
θ range/°	2.237–37.495	2.220–37.499	2.232–37.499	2.252–37.499	2.204–37–498
Absorption correction			Multi-scan		
Transmission (min; max)	0.5761; 0.7484	0.5775; 0.7493	0.5311; 0.7486	0.4946; 0.7536	0.4114; 0.7500
Index range *h*|*k*|*l*	−34/34|−9/9|−31|31	−34/34|−9/9|−31|31	−34/34|−9/9|−31|31	−34/34|−9/9|−31|31	−34/33|−9/9|−32|32
Reflections collected	121 506	52 045	55 272	77 788	59 428
Independent reflections	5191	5323	5253	5076	5270
Obs. reflections	4524	4676	4462	4480	4894
Refined parameter/restraints	177	182	184	178	183
R_{int}	0.0871	0.0536	0.0871	0.0762	0.0514
R_1 (all data)	0.0706	0.0279	0.0499	0.0530	0.0270
wR_2	0.1435	0.0514	0.0952	0.1334	0.0534
GooF	1.294	1.060	1.138	1.148	1.095
Site occupation scenario A	0.7929(17)	0.9322(7)	0.8017(12)	0.7231(15)	0.9028(9)
Site occupation scenario B	0.2071(17)	0.0678(7)	0.1983(12)	0.2769(15)	0.0972(9)
Residual electron density (max; min)/e$^-$ Å^{-3}	4.772; −2.506	2.133; −0.927	2.398; −1.579	5.543; −0.503	3.679; −1.767
CCDC	2376268	2376269	2376271	2376270	2376272

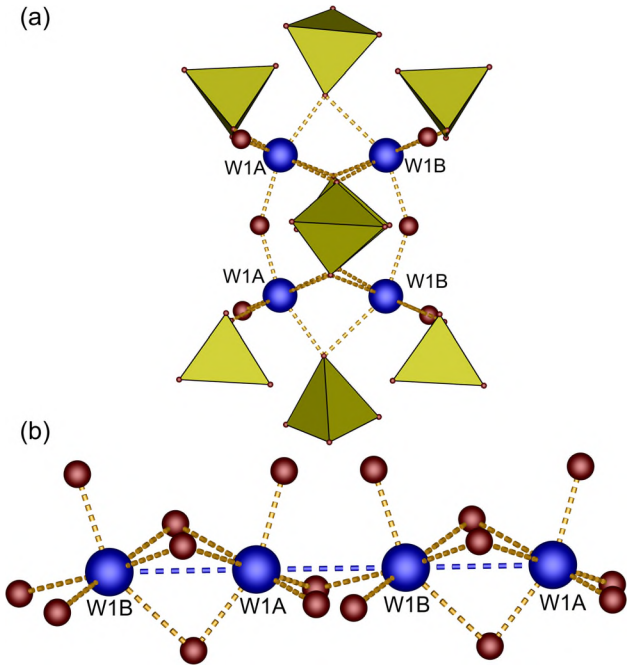

Fig. 2 Scheme of the disorder of the fundamental building unit (a) and the thread-like arrangement of disordered tungsten cations along the *b*-axis (b); W1A represents the position with higher probability.

calculated by the method of Balić-Žunić and Makovicky.[16,17] The tungstate octahedra in $Bi_2[W_2O_3(SO_4)_6]$, centred by W1A show a deviation of −4.47% towards an octahedron (Table S4 in the ESI†). Conversely, those tungstate octahedra centred by W1B exhibit an even larger deviation of −15.16%. In fact, a local order can be expected, otherwise the tungsten cations would come too close to each other as then the octahedra would share common faces. However, the local order is probably below the coherence threshold of the X-ray radiation and therefore cannot be resolved by single-crystal X-ray diffraction. We also did not observe any diffuse scattering.

As all sulfate tetrahedra are connected to both disordered tungstate moieties, they astonishingly do not show disorder. Their polyhedron deviation is remarkably small with −0.11% ($S1O_4^{2-}$), −0.05% ($S2O_4^{2-}$) and −0.04% ($S3O_4^{2-}$). Thus, they can be classified as regular tetrahedra. The oxygen atoms of the sulfate tetrahedra are further coordinated to either three metal cations and one tungsten cation ($S1O_4^{2-}$, $S2O_4^{2-}$) or two metal and two tungsten cations of the respective A or B scenarios ($S3O_4^{2-}$). In the sulfate tetrahedra, there is a slight increase in S–O bond lengths when oxygen coordinates towards the tungsten cation.

This is likely due to the greater repulsion between the central cations exhibiting high oxidation numbers in $[SO_4]^{2-}$ and $[WO_6]^{6-}$. A high repulsion between cations with high charge and low coordination number was already predicted by Pauling's third rule.[18] An elongation due to the same reason is observed in the W–O bonds in the tungstate octahedra, with the shortest distance towards the terminating oxygen ligand and longer bonds towards the bridging oxygen atoms. Selected bond lengths and angles are given in Table 2. The average Bi–O bond length is 243 pm, which is slightly below the expected length of 252 pm according to Shannon's ionic radii considering an eight-fold coordination for bismuth.[19] The angle between the tungstate octahedra is 147.67(2)° for scenario A and 144.52(10)° for scenario B. This resembles the angle of approximately 145° within $[W_2O_3(PO_4)_2]$ units.[20]

Table 2 Selected interatomic distances (pm) and angles (°) in $Bi_2[W_2O_3(SO_4)_6]$. Standard deviations are given in parentheses

Bi–O	225.5(3)–252.2(3)
$\sum r_{ion}$(Bi–O)	252
W1A–$O^{br.}$	189.3(1)–222.0(3)
W1A–$O^{term.}$	168.3(3)
S–$O^{br.}$	147.4(3)–153.9(3)
S–$O^{term.}$	143.2(4)–146.1(3)
O–S–O	104.7(2)–114.5(2)
O–W1A–O	77.09(11)–178.7(1)

For the first time, phase-pure crystalline powders of $M_2[W_2O_3(SO_4)_6]$ (M = Lu, Y, Tb, Eu, Bi) have been successfully synthesised. The corresponding powder X-ray diffraction patterns are shown in Fig. 3, with no side phases observed. As expected, an increase in the metal cation's radii results in a shift of the reflections towards smaller angles, owing to Bragg's law. For M = Lu, Y, and Tb, a broadening of the reflections around 2θ = 17° is noticed, which corresponds to the lattice plane distances of about 5.2 Å. This distance is approximately equal to the distance between two fundamental building units. As shown in Table 1, the site occupation factor of the less likely B scenario increases for the compounds with M = Lu, Y, and Tb and the disorder also increases, which could lead to the observed broadening of the respective reflections. The site occupation factors for the B scenario for the europium and bismuth compounds are remarkably small, resulting in a lack of broadening. This observation correlates with the ionic radii of the metal cation, as europium and bismuth exhibit the largest ionic radii of the discussed compounds.

Electrostatic calculations

Electrostatic consistency was demonstrated by calculations based on the Madelung Part of Lattice Energy (MAPLE) concept.[21–23] The single-crystal data for $M_2[W_2O_3(SO_4)_6]$ (M = Lu, Y, Tb, Eu, Bi) were used to compute the MAPLE values, which were then compared with the summation of the corresponding binary compounds (Table 3). As $M_2[W_2O_3(SO_4)_6]$ features a disorder between scenarios A and B, both MAPLE values were calculated for the pure scenarios. Deviations remain close to or even below 1%, indicating electrostatic consistency of the structure model. In comparing A and B, the A scenarios consistently exhibit a higher MAPLE value, indicating that A is more stable than B. This observation also suggests a higher site occupancy factor for the A scenario (Table 1). This seems plausible considering the mean distance between tungsten and metal cations. While the Bi–W distance in A is approximately 539 pm, B with 537 pm exhibits a smaller distance next to a wider range

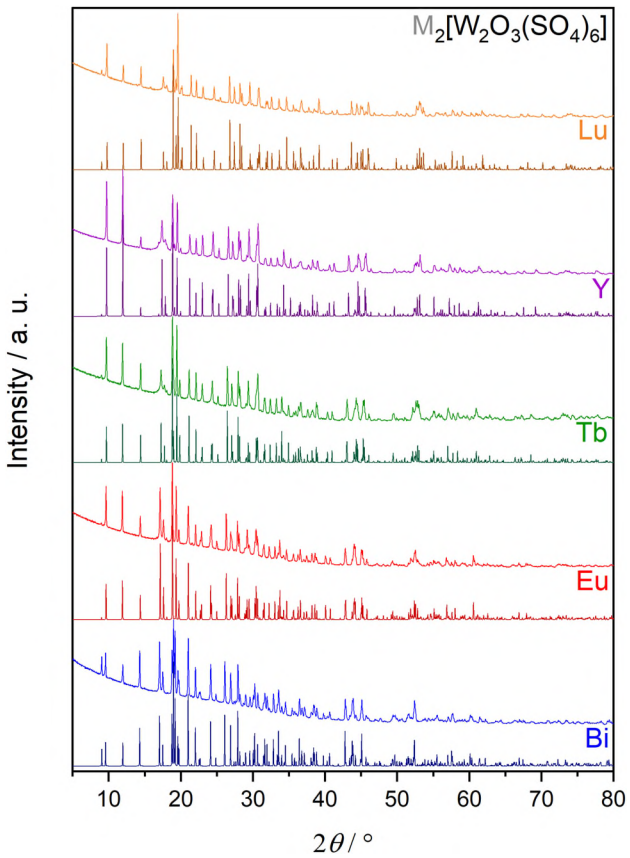

Fig. 3 Experimental powder X-ray diffraction pattern of $M_2[W_2O_3(SO_4)_6]$ (M = Lu, Y, Tb, Eu, Bi) compared to the respective calculated patterns obtained using single-crystal X-ray diffraction.

between the shortest and the longest Bi–W distance. This observation also holds for the other metal cations M without any lone-pair effect. Thus, in scenario A the structure stabilizes due to less repulsion between the metal cations M–W. Moreover, the B scenario figures show stronger electrostatic interactions than the binary compounds, while the A scenario throughout shows weaker ones.

UV-vis and vibrational spectroscopy

To investigate the optical properties of $M_2[W_2O_3(SO_4)_6]$ (M = Lu, Y, Tb, Eu, Bi), UV-vis spectra were recorded for the first time for sulfatotungstates in general. The recorded spectra confirm that the title compounds are colourless as they reflect incident light throughout the visible region (Fig. 4a). In addition, $Eu_2[W_2O_3(SO_4)_6]$ exhibits typically weak f–f transitions of Eu^{3+} cations.[30] Notably, the artefact at 350 nm marks the lamp switch of the device as it changes from the UV to the visible. However, the absorption edge in this region is clearly observed in all compounds and is dominated by charge transfer transitions within the tungstate octahedra. Subsequent photoluminescence measurements show that there is neither any energy transfer onto activators such as Eu^{3+} or Tb^{3+}, nor can any O → M charge transfers be observed for these ions. The band gaps determined *via* Tauc plots[31,32] do not show a simple correlation to the electronegativity of the metal cation M or its radius (Fig. 4b and S6†).[33] $Bi_2[W_2O_3(SO_4)_6]$ has the smallest band gap, while $Tb_2[W_2O_3(SO_4)_6]$ has the largest among the compounds investigated in this work.

The infrared spectra depicted in Fig. 4c indicate the absence of any O–H vibrations in these structures as there are no bands detected in the region between 4000 and 1400 cm^{-1} (Fig. S3†). Moreover, all compounds exhibit comparable spectra due to identical structural motifs, except for M = Bi, where certain bands at higher wavenumbers seem to be shifted to lower energies. The assignment of the bands was made by comparison with the sulfates and tungstates that have been researched and calculated to date.

Bands ranging from 1400 to 950 cm^{-1} can be assigned to typically symmetric ν_{sym}(S–O) and asymmetric ν_{asym}(S–O) stretching vibrations of sulfate tetrahedra, while the first band between 1360 and 1300 cm^{-1} shifts with the ionic radius of the metal cation with lower wavenumbers for bismuth and higher wavenumbers for lutetium. A similar shift can be observed in $M_2[B_2(SO_4)_6]$.[8,34] Bending vibrations δ(S–O) occur in the region between 650 and 400 cm^{-1}.[35–37] In addition, typical stretching vibrations ν_{sym}(W–O) and ν_{asym}(W–O) in tungstate octahedra are found between 960 and 600 cm^{-1}.

Table 3 Calculated MAPLE values of $M_2[W_2O_3(SO_4)_6]$ (M = Lu, Y, Tb, Eu, Bi); values marked with A indicate the disorder including W1A, while values for B are assigned to the disorder with W1B

$Lu_2[W_2O_3(SO_4)_6]$ (SC-XRD) **A:** MAPLE = 247 431 kJ mol^{-1} Δ = 0.55%	**B:** MAPLE = 242 689 kJ mol^{-1} Δ = −1.80%	Lu_2O_3 [24] + 2 WO_3 [25] + 6 SO_3 [26] MAPLE = 247 061 kJ mol^{-1}
$Y_2[W_2O_3(SO_4)_6]$ (SC-XRD) **A:** MAPLE = 249 744 kJ mol^{-1} Δ = 1.20%	**B:** MAPLE = 243 889 kJ mol^{-1} Δ = −1.17%	Y_2O_3 [27] + 2 WO_3 [25] + 6 SO_3 [26] MAPLE = 246 741 kJ mol^{-1}
$Tb_2[W_2O_3(SO_4)_6]$ (SC-XRD) **A:** MAPLE = 248 334 kJ mol^{-1} Δ = 0.71%	**B:** MAPLE = 243 642 kJ mol^{-1} Δ = −1.20%	Tb_2O_3 [24] + 2 WO_3 [25] + 6 SO_3 [26] MAPLE = 246 565 kJ mol^{-1}
$Eu_2[W_2O_3(SO_4)_6]$ (SC-XRD) **A:** MAPLE = 248 251 kJ mol^{-1} Δ = 0.78%	**B:** MAPLE = 245 776 kJ mol^{-1} Δ = −0.22%	Eu_2O_3 [28] + 2 WO_3 [25] + 6 SO_3 [26] MAPLE = 246 319 kJ mol^{-1}
$Bi_2[W_2O_3(SO_4)_6]$ (SC-XRD) **A:** MAPLE = 248 346 kJ mol^{-1} Δ = 0.93%	**B:** MAPLE = 245 686 kJ mol^{-1} Δ = −0.14%	Bi_2O_3 [29] + 2 WO_3 [25] + 6 SO_3 [26] MAPLE = 246 040 kJ mol^{-1}

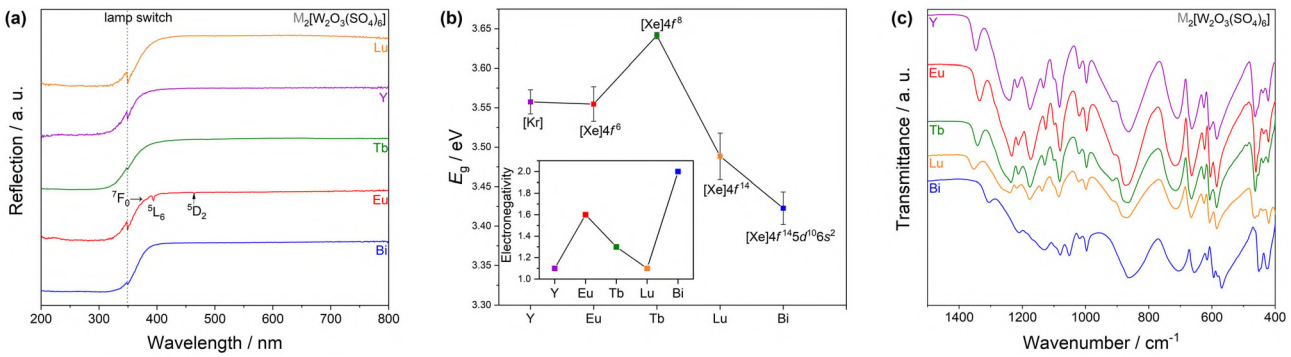

Fig. 4 UV-vis spectra (a) and band gaps (b) of $M_2[W_2O_3(SO_4)_6]$ (M = Lu, Y, Tb, Eu, Bi) determined using Tauc plots (see Fig. S6 in the ESI†) of the UV-vis data and their relationship to electronegativity according to Allen[33]. FT-IR spectra (c) for $M_2[W_2O_3(SO_4)_6]$ (M = Lu, Y, Tb, Eu, Bi).

Shorter bonds between tungsten and oxygen vibrate at higher frequencies, and hence at higher wavenumbers of around 950 cm^{-1}, which applies to the terminal oxygen atoms in the octahedra.[38,39] Furthermore, stretching vibrations between corner-sharing tungsten octahedra ν(W–O–W) are found between 870 and 610 cm^{-1}. The bending vibrations δ(W–O) are located below 500 cm^{-1}.

Fluorescence spectroscopy

Further investigations into the optical properties of $M_2[W_2O_3(SO_4)_6]$ were conducted by recording the photoluminescence spectra for M = Eu, Tb and M = Y doped with 7% Eu^{3+}. The excitation and emission spectra are of particular interest as there are currently no reported luminescence properties for sulfatotungstates. All three compounds exhibit f–f transitions characteristic of their respective rare-earth ion (Fig. 5). Bands are assigned to the term symbols and their transition energy.[30,40,41] The luminescence of Eu^{3+} (Fig. 5a and b) displays a dominant emission line at around 615 nm, identified as the hypersensitive transition $^5D_0 \rightarrow {}^7F_2$.[40] This transition becomes prevalent in non-centrosymmetric surroundings as observed in $M_2[W_2O_3(SO_4)_6]$, where the site symmetry of Eu^{3+} is 1. Notably, the transition $^5D_0 \rightarrow {}^7F_0$ is visible with weak intensity. Although typically this is strictly forbidden, the induced electric dipole transition could be observed in coordination surroundings with low symmetry such as C_n, C_{nv}, and C_s due to possible J-mixing.[40] The presence of only one single site for Eu^{3+} at this position confirms the structure refinement from single-crystal data for the title compounds since only one peak is present. Close to this transition, the magnetic dipole transition $^5D_0 \rightarrow {}^7F_1$ is visible, which is in general independent of any symmetry. C_1 symmetry within the surroundings of Eu^{3+} is expected to cause this transition to divide into three sub-levels.[40] However, only two sub-levels are resolved, probably due to peak overlap. The transition $^5D_0 \rightarrow {}^7F_3$ exhibits weak intensity, as it is forbidden after following the Judd–Ofelt theory, as is the $^5D_0 \rightarrow {}^7F_0$ transition. The last observed transition $^5D_0 \rightarrow {}^7F_4$ is dependent on the coordination environment and displays a relatively high intensity. A regular square antiprism with D_{4d} symmetry would be expected to have dominant intensity for this transition.[40] However, since there is an inversion centre in D_{4d} symmetry, the hypersensitive transition should have low intensity. However, the emission spectra shown in Fig. 5a and b reveal that the hypersensitivity transition has the highest intensity. Thus, the spectra coincide with the coordination environment of the distorted square antiprism of the metal cations by showing the highest intensity for the $^5D_0 \rightarrow {}^7F_2$ transition due to the absence of an inversion centre, but still show the relatively high intensity of the $^5D_0 \rightarrow {}^7F_4$ transition. A comparable emission spectrum was observed for $Eu_2[B_2(SO_4)_6]$, which exhibits a similar Eu^{3+} environment.[8] In general, the luminescence intensity, regard-

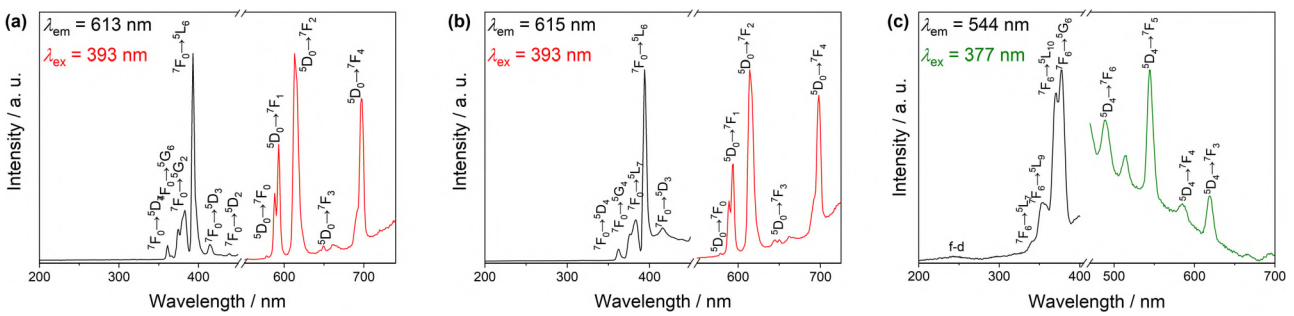

Fig. 5 Emission and excitation spectra of $Eu_2[W_2O_3(SO_4)_6]$ (a), $Y_2[W_2O_3(SO_4)_6]$ doped with 7% Eu^{3+} (b) and $Tb_2[W_2O_3(SO_4)_6]$ (c); due to overcorrection for the lamp intensity at lower wavelengths, the excitation spectra are depicted as non-corrected spectra.

less of whether it is doped or not, appears to be very low when compared to that of other compounds containing sulfates.[8,9,42] A low emission intensity is also noted for M = Tb in Fig. 5c. The $^5D_4 \rightarrow {}^7F_5$ transition is responsible for the highest emission intensity that produces green luminescence.[41] The emission detected at around 514 nm cannot be assigned to any f–f transition of Tb^{3+} or other rare-earth elements. However, the artefact for Tb^{3+} was observed previously in other compounds when excited at 377 nm.[2]

It is worth noting that there is a lack of any charge transfer transition *via* O → Eu, O → Tb or O → W in the excitation spectrum. Such transitions are parity allowed and should therefore be intense. For instance, the charge transfer excitation for WO_6 moieties should be anticipated in the region of 310 nm.[43] Thus, an antenna effect from the tungstate moieties towards the rare-earth cations could not be observed here, probably also due to large distances between tungsten and rare-earth cations. Since all oxygen anions coordinating with the rare-earth cation belong to sulfate units, an energy transfer from the tungstate as necessary for the antenna effect seems to be less likely. However, a weak band at around 245 nm is present in the excitation spectrum due to f–d transitions in Tb^{3+}. This band at relatively high energies indicates rather weak ligand field splitting and thus, weak coordination behaviour, as expected for sulfatotungstates. Other weakly coordinating structures, such as sulfates or borosulfates, show bands in the same region like, *e.g.* 212–254 nm in $Tb_2[B_2(SO_4)_6]$ and 224–258 nm in $Tb(HSO_4)(SO_4)$.[8,9]

Thermal analysis

The thermal stability of $M_2[W_2O_3(SO_4)_6]$ was assessed by TGA (thermal gravimetric analysis) carried out under a nitrogen atmosphere, with thermal treatment up to 1050 °C (Fig. 6 and S10†). At first, an initial mass loss of around 1 to 2% resulted from the evaporation of adherent sulfuric acid. Borosulfates synthesised using oleum showed similar behaviour.[44] All compounds displayed a comparable decomposition pattern, except for M = Bi, which exhibited slight deviations. Those compounds with the metals M = Lu, Y, Tb, and Eu show the same behaviour as that illustrated in Fig. 6 with $Eu_2[W_2O_3(SO_4)_6]$ serving as a representative sample. The decomposition process occurs in two distinct steps according to chemically reasonable reactions (eqn (1) and (2)). TGA measurements for M = Lu, Y, and Tb are shown in Fig. S7–S9.† Both reaction steps release three SO_3 molecules, which are expected to further decompose to SO_2 and O_2.[45] The decomposition temperature decreases as the ionic radius of the metal cation increases (Table 4), and this observation also applies to the pure metals:[46,47]

$$Eu_2[W_2O_3(SO_4)_6] \rightarrow \text{“}Eu_2[W_2O_6(SO_4)_3]\text{”} + 3\ SO_3\ (g) \quad (1)$$

$$\text{“}Eu_2[W_2O_6(SO_4)_3]\text{”} \rightarrow Eu_2W_2O_9 + 3\ SO_3\ (g) \quad (2)$$

The initial decomposition step of eqn (1) begins at around 430 °C for M = Eu, defining the compound's thermal stability. As a result of the absence of crystal water, the compounds feature a comparatively high thermal stability. The observed mass loss of 19.2 wt% aligns well with the estimated weight loss of $\Delta m_{calc.}$ = 18.5 wt%. The thermal decomposition data for all compounds are presented in Table 4. The following step at around 630 °C is split into two processes most likely releasing two SO_3 molecules at first and then another SO_3 with $Eu_2W_2O_9$[47] as the final product, as verified by powder X-ray diffraction and FT-IR measurements (Fig. S10 and S11†). Again, the calculated mass loss of 18.5 wt% is closely matched by the observed loss of 19.3 wt%. The TGA measurement in our study differs from that of a previous study,[15] as they observed an additional decomposition step below 400 °C.[15] This step is presumably linked to the decomposition of an $Eu(S_2O_7)(HSO_4)$ side phase and not to the release of SO_3.[42] Therefore, it can be inferred that the investigated sample of $Eu_2[W_2O_3(SO_4)_6]$ contained $Eu(S_2O_7)(HSO_4)$ in the prior work. The phase purity of our compounds was proven by powder X-ray diffraction and FT-IR analysis, validating the suitability of the TGA steps shown in Fig. 6.

$Bi_2[W_2O_3(SO_4)_6]$ also undergoes two decomposition steps but appears to deliver a different product under the same

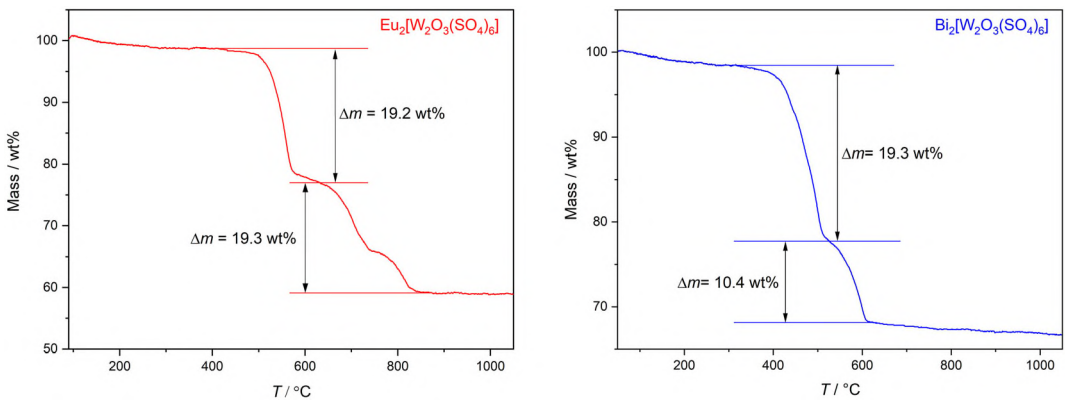

Fig. 6 Thermograms of $Eu_2[W_2O_3(SO_4)_6]$ (left panel) and $Bi_2[W_2O_3(SO_4)_6]$ (right panel) recorded up to 1050 °C in a nitrogen atmosphere.

Table 4 Suggested decomposition steps during the TGA measurement; T_1 indicates the first decomposition step and T_2 the second step

Compound	T_1	Decomposition product	T_2	Decomposition product
$Lu_2[W_2O_3(SO_4)_6]$	510 °C $\Delta m_{calc.}$ = 17.9% $\Delta m_{obs.}$ = 19.1%	"$Lu_2[W_2O_6(SO_4)_3]$"	660 °C $\Delta m_{calc.}$ = 17.9% $\Delta m_{obs.}$ = 17.9%	$Lu_2W_2O_9$
$Y_2[W_2O_3(SO_4)_6]$	450 °C $\Delta m_{calc.}$ = 20.5% $\Delta m_{obs.}$ = 24.5%	"$Y_2[W_2O_6(SO_4)_3]$"	645 °C $\Delta m_{calc.}$ = 20.5% $\Delta m_{obs.}$ = 21.9%	$Y_2W_2O_9$
$Tb_2[W_2O_3(SO_4)_6]$	440 °C $\Delta m_{calc.}$ = 18.3% $\Delta m_{obs.}$ = 18.8%	"$Tb_2[W_2O_6(SO_4)_3]$"	630 °C $\Delta m_{calc.}$ = 18.3% $\Delta m_{obs.}$ = 19.5%	$Tb_2W_2O_9$
$Eu_2[W_2O_3(SO_4)_6]$	430 °C $\Delta m_{calc.}$ = 18.5% $\Delta m_{obs.}$ = 19.2%	"$Eu_2[W_2O_6(SO_4)_3]$"	630 °C $\Delta m_{calc.}$ = 18.5% $\Delta m_{obs.}$ = 19.2%	$Eu_2W_2O_9$
$Bi_2[W_2O_3(SO_4)_6]$	320 °C $\Delta m_{calc.}$ = 17.0% $\Delta m_{obs.}$ = 19.3%	"$Bi_2[W_2O_6(SO_4)_3]$"	530 °C $\Delta m_{calc.}$ = 10.4% $\Delta m_{obs.}$ = 11.4%	"$Bi_2[W_2O_8(SO_4)]$"

thermal treatment. Reasonable reaction equations are as follows:

$$Bi_2[W_2O_3(SO_4)_6] \rightarrow \text{“}Bi_2[W_2O_6(SO_4)_3]\text{”} + 3\ SO_3\ (g) \quad (3)$$

$$\text{“}Bi_2[W_2O_6(SO_4)_3]\text{”} \rightarrow \text{“}Bi_2[W_2O_8(SO_4)]\text{”} + 2\ SO_3\ (g) \quad (4)$$

The first decomposition step behaves similarly to that for $Eu_2[W_2O_3(SO_4)_6]$, releasing three SO_3 molecules with an observed mass loss of 19.3 wt%, which is relatively close to $\Delta m_{calc.}$ = 17.0 wt%. Nevertheless, the decomposition has already started at around 320 °C. The second step at 530 °C does not occur in two stages and only two SO_3 molecules are released revealing $Bi_2[W_2O_8(SO_4)]$ as the final product. Again, the observed mass loss of 10.4 wt% is close to $\Delta m_{calc.}$ = 11.4 wt%. Further release of SO_3 is anticipated to occur at even higher temperatures.

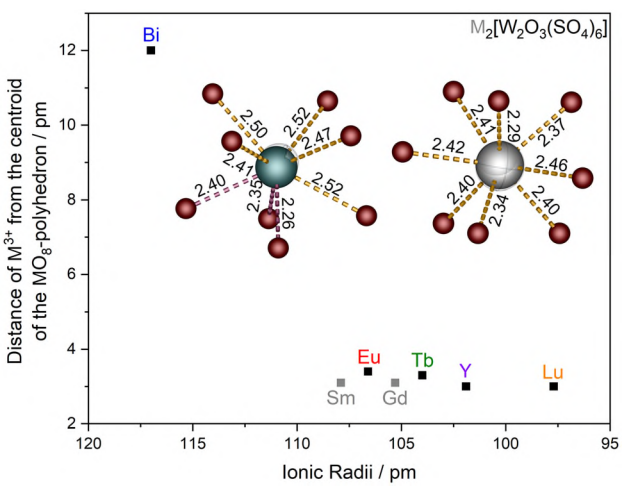

Fig. 7 Lone-pair activity of bismuth compared to europium and isotypic compounds; data taken from published data (greyscale labels; for refs., please see text). The resulting tripod in the coordination with bismuth (on the left) is demonstrated by violet bonds; in contrast, europium shows no lone-pair activity (on the right).

Lone-pair effect

The coordination behaviour of the bismuth compound differs from that of the other metals due to the activity of its lone pair.[48–51] In comparison to the other metal cations within these isotypic compounds, bismuth has a considerably greater distance from the centroid R_c, calculated through the method of Balić-Žunić and Makovicky (Fig. 7).[16,17] This is attributed to the lone pair being directed towards the longer bonds, while the shortest bonds in the opposite direction form a tripod due to the orientation of the p-orbitals. The O–Bi–O angles in the tripod measure 71.0°, 88.6°, and 71.7°, whereas angles close to 90° are expected due to the p-character.[48] In contrast, the europium cation shows no pronounced behaviour, as the bond lengths are distributed uniformly. The eccentricity ε is utilized to categorize the centroid deviation independently of various coordination numbers, providing an example where a lone pair can be either quenched or expressed.[48] A larger ε value signifies a more expressed lone pair and, therefore, has a greater stereochemical influence on its surroundings. This is defined as the ratio between the centroid deviation R_c and the radius of the enclosing sphere. $Bi_2[W_2O_3(SO_4)_6]$ has an eccentricity value of ε = 0.048, indicating that bismuth indeed shows an expressed lone-pair activity. However, compared to other sulfates or tungstates, its influence appears to be relatively small as in, *e.g.* Bi_2WO_6 (ε = 0.164) and $Bi_2(SO_4)_3$ (ε = 0.136).[48,52]

Experimental section

Synthesis

$M_2[W_2O_3(SO_4)_6]$ (M = Lu, Y, Tb, Eu, Bi) were prepared *via* solvothermal syntheses. Initially, M_2O_3 and $WOCl_4$ were loaded into a silica ampoule of 1 cm diameter and 14 cm length followed by the addition of oleum (0.5 ml, Merck, 65% SO_3). The ampoule was torch-sealed, and the following temperature program was applied. First, it was heated up to 310 °C for 3 h, held at this temperature for 24 h and cooled again to room temperature within 24 h. Afterwards, the ampoules were

flipped to separate the crystals from the mother liquor before they were opened. Colourless, single crystals were formed in the acid. Due to their sensitivity to moisture, the crystals were washed multiple times with acetonitrile under a nitrogen atmosphere. *Caution*: During and after the reaction the ampoules must be handled with great care since they are under remarkable pressure. Thus, it is recommended that they are cooled with liquid nitrogen before opening. The crystals were transferred and stored in a glovebox filled with argon.

X-ray powder diffraction

The samples were ground in an argon-filled glovebox and filled in a Hilgenberg silica-glass capillary with a wall thickness of 0.01 mm and an outer diameter of 0.3 mm. Data were collected by means of a Bruker D8 Advance diffractometer using Cu-K_α radiation (λ = 1.54184 Å) with a 1D LynxEye detector system, steps of 0.02° and transmission geometry. The generator was operated at 40 kV and 40 mA. At lower diffraction angles, a background signal is visible in the measurement which is assigned to the absorption of the glass capillary.

The samples after thermal treatment were measured with a Seifert 3003 TT diffractometer in the Bragg–Brentano geometry at room temperature while using Cu-K_α radiation (λ = 1.54184 Å) with a GEMETEOIR 1D line detector. A Ni filter suppresses K_β radiation. The X-ray tube was operated at 40 kV and 40 mA over a scan range between 5 and 80° at an increment of 0.02°. The samples were ground, transferred to a stainless-steel sample holder and flattened with a glass plate.

Single-crystal structure determination

Single crystals were transferred from the ampoule into a perfluorinated polyether to enable selection for single-crystal X-ray diffraction. Diffraction data were collected by means of a Bruker D8 Venture diffractometer while using Mo-K_α radiation (λ = 0.71073 Å). The temperature was adjusted with a nitrogen flow using an Oxford cryosystem. The absorption correction was done by the multi-scan method, after which direct methods were used to solve the crystal structures followed by refinement by the full-matrix least-squares technique within the SHELXTL software package.[53,54] The disordered scenarios A and B were refined by using the command PART with W1A, O1A, O2A as PART 1 and W1B, O1B, O2B as PART 2. Relevant crystallographic data and further details of the structure determination for $Bi_2[W_2O_3(SO_4)_6]$ are summarised in Tables 2, S1 and S2.†

Due to the systematic disorder of the electron-rich tungsten atoms the refinements unfortunately show some selected weird residual electron densities and a few weird ADPs. But, by also considering all data, the subsequent Rietveld refinement, and especially our explanation for this disorder and its trend among the presented compounds, it is obvious that in these cases the single-crystal X-ray diffraction, and therefore also any refinement, cannot resolve this disorder properly.

Rietveld analysis of $Eu_2[W_2O_3(SO_4)_6]$ was performed using the TOPAS V. 5.0 program.[55] The structural model out of single-crystal data was used as the starting model. Details of the Rietveld refinement are displayed in Fig. S12 and Table S3.†

Further details of the crystal structure may be obtained from the Fachinformationszentrum Karlsruhe, 76344 Eggenstein-Leopoldshafen, Germany, on quoting the deposition no. CCDC 2376268 through 2376272† as indicated in Table 1.

Infrared spectroscopy

Infrared spectra were recorded with a Bruker EQUINOX 55 FT-IR spectrometer at room temperature while using a platinum ATR device with a scan range between 4000 and 400 cm^{-1}, a resolution of 2 cm^{-1} and running 32 scans per sample.

UV-vis spectroscopy

The UV-vis spectra were recorded as diffuse reflection spectra using a Varian Cary 300 Scan UV-vis spectrophotometer with an Ulbricht sphere detector and a deuterium and mercury lamp as the light source (lamp switch at 350 nm). The scan range was between 200 and 800 nm with an increment of 1 nm and a scan rate of 120 nm cm^{-1}.

Photoluminescence

The solid-state excitation and emission spectrum was recorded using a Horiba FluoroMax-4 fluorescence spectrometer operating at room temperature. The spectrometer is equipped with a xenon discharge lamp operating between 200 and 800 nm. The excitation spectrum was corrected with respect to the lamp intensity.

Thermal analysis

Thermogravimetric analysis (TGA) measurements were performed using alumina crucibles with a NETZSCH STA 409 PC Luxx under a nitrogen atmosphere with a heating ramp of 5 °C min^{-1}.

Conclusions

This study elucidates sulfatotungstates $M_2[W_2O_3(SO_4)_6]$ (M = Y, Eu, Tb, Lu, Bi) by introducing various new metal cations into the structure. Phase-pure powders of the title compounds were received and examined with respect to their crystal structure, and optical and thermal properties. Single-crystal X-ray diffraction revealed a disorder in the tungsten ions with a preferred occupation A, which was confirmed by MAPLE calculations.

Fluorescence spectroscopy confirmed the distorted square antiprismatic coordination of the metal cations M, showing red luminescence for Eu^{3+} with a dominant intensity due to the hypersensitive transition $^5D_0 \rightarrow {}^7F_2$. The weak green emission for the terbium compound originates mainly from the $^5D_4 \rightarrow {}^7F_5$ transition. No antenna from the tungstate units was observed due to large distances between the tungsten and the metal cations. The f–d transition of Tb^{3+} at high energies indicates a rather weak coordinating host structure in sulfatotungstates. The band gaps of the compounds were determined

from UV-vis data using Tauc plots, revealing the highest band gap for the terbium compound and the lowest one for the bismuth compound. Additionally, the title compounds showed moderate thermal stability ranging from 320 °C for $Bi_2[W_2O_3(SO_4)_6]$ to 510 °C for $Lu_2[W_2O_3(SO_4)_6]$, as verified by TGA measurements.

Finally, the bismuth compound possesses an expressed lone pair activity with an eccentricity of $\varepsilon = 0.048$, as calculated by the method of Balić-Žunić and Makovicky.[16,17]

Data availability

Data for this article, such as the crystallographic data including CIF files, are available from the ICSD at **https://www.ccdc.cam.ac.uk/structures/**. The respective CCDC numbers are listed in Table 1 of this manuscript. All further data supporting this article have been included as part of the ESI.† Details of the employed software for the investigations presented in our manuscript are given in the Experimental section.

Conflicts of interest

There are no conflicts to declare.

References

1 R. S. Barker, I. Radosavljevic and Evans, *Acta Crystallogr., Sect. B: Struct. Sci.*, 2008, **64**, 708–712.
2 M. Hämmer, O. Janka, J. Bönnighausen, S. Klenner, R. Pöttgen and H. A. Höppe, *Dalton Trans.*, 2020, **49**, 8209–8225.
3 P. V. Klevtsov and R. F. Klevtsova, *J. Struct. Chem.*, 1977, **18**, 339–355.
4 J. Chen, X. Yang, C. Jiang, Y. Wang, L. Zhou and M. Wu, *RSC Adv.*, 2022, **12**, 29338–29345.
5 O. Beaury, M. Faucher and G. Teste de Sagey, *Acta Crystallogr., Sect. B: Struct. Crystallogr. Cryst. Chem.*, 1981, **37**, 1166–1170.
6 M. Daub, A. J. Lehner and H. A. Höppe, *Dalton Trans.*, 2012, **41**, 12121–12128.
7 G. Blasse and A. Bril, *J. Chem. Phys.*, 1966, **45**, 2350–2355.
8 P. Netzsch, M. Hämmer, P. Gross, H. Bariss, T. Block, L. Heletta, R. Pöttgen, J. Bruns, H. Huppertz and H. A. Höppe, *Dalton Trans.*, 2019, **48**, 4387–4397.
9 P. Netzsch, H. Bariss, L. Bayarjargal and H. A. Höppe, *Dalton Trans.*, 2019, **48**, 16377–16383.
10 S. Azuma, T. Kadoguchi, Y. Eguchi, H. Hirabaru, H. Ota, M. Sadakane, K. Yanagisawa, T. Hasegawa and T. Ueda, *Dalton Trans.*, 2020, **49**, 2766–2770.
11 A. L. Paulsen, A. G. Kalampounias, R. W. Berg and S. Boghosian, *J. Phys. Chem. A*, 2011, **115**, 4214–4222.
12 S. Schäffer and R. W. Berg, *Acta Crystallogr., Sect. E: Struct. Rep. Online*, 2005, **61**, i49–i51.
13 K. Ståhl and R. W. Berg, *Acta Crystallogr., Sect. E: Struct. Rep. Online*, 2009, **65**, i88.
14 U. Betke and M. S. Wickleder, *Inorg. Chem.*, 2011, **50**, 858–872.
15 U. Betke and M. S. Wickleder, *Eur. J. Inorg. Chem.*, 2011, **2011**, 4400–4413.
16 T. Balić-Žunić and E. Makovicky, *Acta Crystallogr., Sect. B: Struct. Sci.*, 1996, **52**, 78–81.
17 E. Makovicky and T. Balić-Žunić, *Acta Crystallogr., Sect. B: Struct. Sci.*, 1998, **54**, 766–773.
18 L. Pauling, *J. Am. Chem. Soc.*, 1929, **51**, 1010–1026.
19 R. D. Shannon, *Acta Crystallogr., Sect. A: Cryst. Phys., Diffr., Theor. Gen. Crystallogr.*, 1976, **32**, 751–767.
20 M. Hanawa and H. Imoto, *J. Solid State Chem.*, 1999, **144**, 325–329.
21 R. Hoppe, *Z. Naturforsch.*, 1995, **50**, 555–567.
22 R. Hübenthal, *MAPLE. Program for the Calculation of the Madelung Part of Lattice Energy*, University of Gießen, Germany, 1993.
23 R. Hoppe, *Angew. Chem., Int. Ed. Engl.*, 1966, **5**, 95–106.
24 A. Saiki, N. Ishizawa, N. Mizutani and M. Kato, *Bull. Chem. Soc. Jpn.*, 1985, **93**, 649–654.
25 A. Aird, M. C. Domeneghetti, F. Mazzi, V. Tazzoli and E. K. H. Salje, *J. Condens. Matter Phys.*, 1998, **10**, L569–L574.
26 R. Pascard and C. Pascard-Billy, *Acta Crystallogr.*, 1965, **18**, 830–834.
27 M. G. Paton and E. N. Maslen, *Acta Crystallogr.*, 1965, **19**, 307–310.
28 H. L. Yakel, *Acta Crystallogr., Sect. B: Struct. Crystallogr. Cryst. Chem.*, 1979, **35**, 564–569.
29 G. Malmros, L. Fernholt, C. J. Ballhausen, U. Ragnarsson, S. E. Rasmussen, E. Sunde and N. A. Sørensen, *Acta Chem. Scand.*, 1970, **24**, 384–396.
30 W. T. Carnall, P. R. Fields and K. Rajnak, *J. Chem. Phys.*, 1968, **49**, 4450–4455.
31 J. Tauc, *Mater. Res. Bull.*, 1968, **3**, 37–46.
32 J. Tauc, R. Grigorovici and A. Vancu, *Phys. Stat. Sol.*, 1966, **15**, 627–637.
33 L. C. Allen, *J. Am. Chem. Soc.*, 1989, **111**, 9003–9014.
34 M. Hämmer, L. Bayarjargal and H. A. Höppe, *Angew. Chem., Int. Ed.*, 2021, **60**, 1503–1506.
35 M. V. Barashkov, A. I. Komyak and S. N. Shashkov, *J. Appl. Spectrosc.*, 1999, **1**, 100–104.
36 V. Ramakrishnan, V. U. Nayar and G. Aruldhas, *Infrared Phys.*, 1985, **25**, 607–610.
37 Y. Denisenko, A. S. Aleksandrovsky, V. V. Atuchin, A. S. Krylov, M. S. Molokeev, A. S. Oreshonkov, N. P. Shestakov and O. V. Andreev, *J. Ind. Eng. Chem.*, 2018, **68**, 109–116.
38 C. Guery, C. Choquet, F. Dujeancourt, J. M. Tarascon and J. C. Lassegues, *J. Solid State Electrochem.*, 1997, **1**, 199–207.
39 M. F. Daniel, B. Desbat, J. C. Lassegues, B. Gerand and M. Figlarz, *J. Solid State Chem.*, 1987, **67**, 235–247.
40 K. Binnemans, *Coord. Chem. Rev.*, 2015, **295**, 1–45.

41 W. T. Carnall, P. R. Fields and K. Rajnak, *J. Chem. Phys.*, 1968, **49**, 4424–4442.
42 V. Wessels, S. Kügle and H. A. Höppe, *in preparation*.
43 F. B. Xiong, D. S. Guo, H. F. Lin, L. J. Wang, H. X. Shen and W. Z. Zhu, *J. Alloys Compd.*, 2015, **647**, 1121–1127.
44 P. Netzsch and H. A. Höppe, *Inorg. Chem.*, 2020, **59**, 18102–18108.
45 H. Karasawa and A. Sasahira, *Int. J. Nucl. Hydrogen Prod. Appl.*, 2006, **2**, 134–143.
46 M. Laing, *J. Chem. Educ.*, 2001, **78**, 1054.
47 G. J. McCarthy, R. D. Fischer and J. Sanzgiri, *J. Solid State Chem.*, 1972, **5**, 200–206.
48 M. Hämmer, J. Brgoch, P. Netzsch and H. A. Höppe, *Inorg. Chem.*, 2022, **61**, 4102–4113.
49 M. Atanasov and D. Reinen, *J. Am. Chem. Soc.*, 2002, **124**, 6693–6705.
50 A. Walsh, D. J. Payne, R. G. Egdell and G. W. Watson, *Chem. Soc. Rev.*, 2011, **40**, 4455–4463.
51 W. G. Zeier, A. Zevalkink, Z. M. Gibbs, G. Hautier, M. G. Kanatzidis and G. J. Snyder, *Angew. Chem., Int. Ed.*, 2016, **55**, 6826–6841.
52 A. D. Rae, J. G. Thompson and R. L. Withers, *Acta Crystallogr., Sect. B: Struct. Sci.*, 1991, **47**, 870–881.
53 G. M. Sheldrick, *SHELXTL*, Bruker AXS, Karlsruhe, Germany, 2003.
54 G. M. Sheldrick, *Acta Crystallogr., Sect. C: Struct. Chem.*, 2015, **71**, 3–8.
55 *Topas V5*, Bruker AXS, Karlsruhe, Germany, 2014.